Retrieval and Validation of the Secchi Disk Depth Values (Zsd) from the Sentinel-3 satellite data in the Persian Gulf and the Gulf of Oman

Keivan Kabiri (kabiri@inio.ac.ir)
Iranian National Institute for Oceanonography and Atmospheric Science https://orcid.org/0000-0002-8437-7328

Research Article

Keywords: Remotely Sensed Data, Water Transparency/Clarity, Water Quality, Spatiotemporal Assessment

Posted Date: March 9th, 2023

DOI: https://doi.org/10.21203/rs.3.rs-2547622/v1

Abstract

In this study, the Secchi disk depth (Z_{sd}) values as an indicator of seawater clarity/transparency were estimated using the ESA (European Space Agency) Sentinel-3A and − 3A OLCI (S3/OLCI) satellite data in the Persian Gulf and the Gulf of Oman (PG&GO). To do so, two procedures were evaluated including an empirical methodology developed by Doron et al., 2007 and 2011 and a novel model proposed in this research formed by employing the blue (B_4) and green (B_6) bands of S3/OLCI data. In this regard, a total number of 157 field-measured Z_{sd} values (114 training points for calibration of the models and 43 control points for accuracy assessment of them) were observed during eight research cruises conducted by the research vessel, the Persian Gulf Explorer, in the PG&OS between 2018 and 2022. The optimum methodology was then selected based on the statistical indicators including, R^2 (coefficient of determination), RMSE (root mean square error), and MAPE (mean absolute percentage error). However, after the indication of the optimal model, the data of all 157 observations were utilized for the calculation of unknown parameters of the model. The final results demonstrated that compared to the existing empirical model proposed by Doron et al., 2007 and 2011, the developed model in this study which was formed based on the linear and ratio terms of B_4 and B_6 bands, has more efficiency in the PG&GO. Consequently, a model in form of $Z_{sd} = e^{1.638 B_4/B_6 - 8.241 B_4 - 12.876 B_6 + 1.26}$ was suggested for the estimation of Z_{sd} values from S3/OLCI in the PG&GO (R^2 = 0.749, RMSE = 2.56 m, and MAPE = 22.47%). The results also showed that the annual oscillation of the Z_{sd} values in the GO (5–18 m) is evidently higher compared with those in the PG (4–12 m) and the SH (7–10 m) regions.

1. Introduction

The variations of water transparency/clarity in coastal and offshore areas are assumed as a key measure of water quality, which may have significant impacts on coastal and marine habitats, living resources, and fisheries. Seawater transparency is also continuously affected by different sources of pollutants, both originating in the marine area and flowing from coastal watersheds. This means that such a measure should be regularly evaluated, and then monitored spatiotemporally in environmentally important nearshore and offshore areas (Luis et al., 2019).

The Secchi disk depth (Z_{sd}) is still the simplest measure, and at the same time, the most typical method to quantify water transparency in lakes and inland waters (Swift et al., 2006; McCullough et al., 2012; Ren et al., 2018; Qin et al., 2023) as well as coasts (Kataržytė et al., 2019) and offshore areas (Kabiri, 2022a). The Secchi disk is a white disk for observations in seas and oceanic waters (diameter = 30 cm) or a black and white (B&W) disk for observations in lakes and fresh waters (diameter = 20 cm), attached to a marked sampling rope. Practically, the operator tries to find the disappearance or reappearance of the disk as it lowers into water by a rope, and then record the values in meters. Even though the direct field measurement of the Z_{sd} values provides the most accurate results in detail, it tends to be limited by spatiotemporal coverage due to costs and some other challenges, such as the implementation of observations in remote areas.

A logical solution to deal with the above-mentioned limitations of using in-situ measurements is employing remotely-sensed data (RSD) from satellites to estimate the Z_{sd} values. In doing so, the medium- or low-spatial-resolution satellite data would be a good alternative for field measurements, in which they are in access free of charge, and even have a vast coverage in a single scene. Moreover, the high-temporal resolution (i.e., the short revisit cycle) of relatively lower-spatial-resolution satellite images, such as the National Aeronautics and Space Administration (NASA) Moderate Resolution Imaging Spectroradiometer (MODIS) and the European Space Agency (ESA) Ocean and Land Color Instrument (OLCI) data, are the key benefits of estimating water transparency on a daily basis. In this regard, numerous studies have been so far accomplished to suggest some models for the approximation of the Z_{sd} from the medium-spatial-resolution satellite images (Kloiber et al., 2002; Kabiri and Moradi, 2016; Olmanson et al., 2016; Ren et al., 2018; Kabiri, 2022b; Yang et al., 2022), and the low-spatial-resolution data (Kratzer et al., 2003; Chen et al., 2007; Wu et al., 2008; Doron et al., 2011; Kabiri, 2022a).

While there are some studies on the estimation of the Z_{sd} values from older satellite imagers, such as the MODIS, the Medium Resolution Imaging Spectrometer (MERIS), and the Sea-Viewing Wide Field-of-View Sensor (SeaWiFS) (Doron et al., 2011; Al Kaabi et al., 2016; Kabiri, 2022a), the number of the same investigations reflecting on the Sentinel-3A&B (S3) OLCI (S3/OLCI) sensors is smaller since they have just launched in February 2016 and April 2018, respectively. In spite of this, the models developed for the MERIS are applicable to the OLCI because the MERIS is a precursor for the OLCI with 15 similar spectral bands (viz., the MERIS heritage bands). Generally, the models developed for the estimation of the Z_{sd} values from the satellite images are formed according to the irradiance attenuation coefficient at 490 nm (K_d^{490}), or the ratio values of two bands. As an instance, Alikas and Kratzer (2017) established and compared different empirical and semi-analytical methods to estimate the Z_{sd} values from the MERIS data for the lakes and coastal waters in the Nordic countries, and concluded that it was possible to retrieve accurate water transparency over various optical water types, using the satellite data. Thereafter, Toming et al. (2017) utilized the data of the OLCI imager for mapping some water quality parameters, including the Z_{sd} values in the optically complex waters of the Baltic Sea for both clear and turbid seawaters, with reference to the model proposed by Alikas and Kratzer (2017). They further settled that the models in the form of $(R_{560}/R_{709})^{0.788}\times1.125$ and $(R_{490}/R_{709})^{0.697}\times2.137$, showing the best performance to estimate the Z_{sd} values in the turbid and clear waters from the OLCI imager data, respectively (wherein R_i refers to the atmospherically corrected reflectance values of the band with wavelength = i). Kyryliuk and Kratzer (2019) correspondingly suggested a power model (based on the OLCI values of the irradiance attenuation coefficient at 489 nm) in the form of $Z_{sd}=2.39\times K_d(489)^{-0.86}$ to approximate the Z_{sd} values in the Baltic Sea (RMSE = 62%, Absolute Percentage Difference [APD] = 60%).

However, relatively few studies have been so far fulfilled, particularly in the Persian Gulf and the Gulf of Oman (hereafter, PG&GO), for the approximation of the Z_{sd} values, using the high-temporal resolution of RSD, such as the MODIS or OLCI imagers. For example, two different models have been to date examined to estimate the Z_{sd} values from the MOIDS-K_d^{490} values by Al Kaabi et al. (2013) in the nearshore waters

of Abu Dhabi, the United Arab Emirates, in the southern PG, comprising the K_d^{490} product. In their study, they figured out that the empirical algorithm performance was better, where the mostly K_d^{490}<0.2 m^{-1}, although the semi-analytical algorithm showed better results in which K_d^{490}>0.2 m^{-1}. Thereafter, Al Kaabi et al. (2016) developed a power model in the form of $1.01+(K_d^{490})^{-0.9}$ to calculate Z_{sd} from the MOIDS-K_d^{490} values. Similarly, Kabiri (2022a) proposed a method for the estimation of Z_{sd} from the MOIDS-K_d^{490} in the northern PG&GO, and concluded that the power regression model was optimal (R^2 = 0.81, RMSE = 2.04 m), so the model in the form of $Z_{sd}=0.34\ (K_d^{490})^{-1.42}$ could be applied to compute the Z_{sd} values in the study area.

Generally; it seems that relevant research about the approximation of the Z_{sd} values, using RSD is still rare in the PG&GO, mainly due to the lack of harmonized field matchup data. Therefore, the present study was to correlate the OLCI data with the field-observed Z_{sd} values in the PG&GO. For this purpose, the Z_{sd} values were initially collected during eight cruises operated by the research vessel of the Iranian National Institute for Oceanography and Atmospheric Science (INIOAS), namely, the Persian Gulf Explorer (PGE), in the Iranian waters of the PG&GO from 2018 to 2022. Then, the capabilities of the existing and developed methods together with a novel regional model proposed in this line were evaluated and compared to suggest the optimum one for the estimation of the Z_{sd} values from the OLCI data.

2. Study Area

The whole PG&GO was selected as the study area, wherein eight research cruises had been thus far operated by the PGE, between 2018 and 2022 (Table 1) on the Iranian side of the exclusive economic zone (EEZ) (Fig. 1). Though the bulk of the study area was categorized as the Case-2 waters (i.e., the relatively more turbid waters), some parts of the GO consisted of the Case-1 ones (Kabiri et al., 2022a). Of note, the PG&GO is located in a subtropical, hyper-arid zone that is generally characterized by high temperatures and low precipitation rates (Moradi and Kabiri, 2015). The climate of the PG is mainly influenced by the Mediterranean systems, while the GO is more affected by the Indian Ocean Monsoon. The mean annual rainfall on the southern coasts and over the PG&GO is ~ 100 mm, while it is ~ 355 in the northern parts (Kabiri et al., 2013; Kabiri et al., 2018; Beni et al., 2021). The current energy in the upper layers of the PG&GO has two peaks per year, one from late winter to early spring and another one from late summer to early fall, which means it grows during winter monsoons (Akhyani et al., 2015). Previous studies have further reported that the annual variation range of the Z_{sd} values in the GO has been higher than that in the PG, so the maximum and minimum water transparency have occurred in warm and colder ones, respectively (Kabiri, 2022a).

Table 1. The detailed information of field-observed Z_{sd} values through eight cruises operated by the research vessel, the PGE, in the PG&GO

No.	Cruise name	Start date	End date	No. of observed Z_{sd}	Z_{sd} range (m)
1	PGE1801	1/Jan/2018	7/Jan/2018	8	1.5 – 19.0
2	PGE1802	16/May/2018	21/May/2018	14	1.5 – 18.0
3	PGE1803	19/Sep/2018	3/Oct/2018	11	10.0 – 18.0
4	PGE1804	20/Dec/2018	22/Dec/2018	6	6.0 – 16.0
5	PGE1901	2/May/2019	13/May/2019	29	1.5 – 18.0
6	PGE1902	12/Nov/2019	13/Nov/2019	5	4.5 – 15.0
7	PGE2102	6/Sep/2021	30/Sep/2021	41	1.5 – 20.0
8	PGE2201	12/Jan/2022	12/Feb/2022	43	1.5 – 20.0

3. Materials And Methods

3.1. Field Observations

The field Z_{sd} values were collected during eight research cruises operated by the PGE, in the Iranian waters of the PG&GO between 2018 and 2022 (Table 1). These cruises had been practiced in a total number of 66 main points (namely, MP_x in Fig. 1, x = point number), which were typically repeated in cruises, and also 28 ancillary points (viz., AP_y in Fig. 1, y = point number), which were occasionally selected in some cruises for filling the spatial gaps between the points. It should be noted that the Z_{sd} readings needed to be completed two hours after sunrise and two hours before sunset, and on the shadow side of the vessel to avoid any light noises and glints caused by water surface reflections (Tyler, 1968). Therefore, the number of the Z_{sd} observations was limited to the points measured during the daytime in all cruises. Consequently, 157 Z_{sd} values in total were observed in 94 stations (i.e., some points were measured in more than one cruise). In this study, it was decided to select 114 Z_{sd} values surveyed in the first seven cruises (viz., the PGE1801-1804, the PGE1901-1902, and the PGE2102) for the calibration of the nominated models, and the rest 43 observations in the eighth cruise (namely, the PGE2201) for the accuracy assessment and validation of the results (Fig. 1, Table 1).

3.2. Remotely Sensed Data

The S3 (A&B) spacecrafts were launched in February 2016 and April 2018, respectively, both carrying the same four main instruments. Among the data, the level-1 data of the OLCI were particularly selected for this study (hereafter called, S3/OLCI), in conformity with the aforementioned field-observed data, and then downloaded from the Copernicus Open Access Hub (https://scihub.copernicus.eu/). Notably, the data of some dates were not applicable, mostly due to the cloudy situation; hence, they were replaced

with the closest date available. In this regard, it was decided that the time interval between the field-observed Z_{sd} values and the satellite data to be three days or less to minimize the effects of the variations in water quality in the study area on further computations. This difference could be seven days for the lake areas as suggested in previous studies (Olmanson et al., 2008; McCullough et al., 2012); however, this might not be valid for more dynamic areas, such as the PG&GO, wherein the variation rate of water quality was quite higher than lakes. In practice, most of the OLCI data utilized in this study and the associated field-observed Z_{sd} values were for the same day, and their mean difference was less than two days.

3.3. Satellite Image Analysis

Typically, all analyses based on satellite images include three steps, viz., pre-, main-, and post-processing. At the pre-processing steps, the required corrections, such as radiometric, atmospheric, and even geometric ones, should be applied to raw satellite data before they are utilized at the main-processing step, which contains using or developing algorithms to extract the required data (here, the Z_{sd} values) from the corrected satellite images, and usually employing the relevant field-measured/observed data. Consequently, the accuracy and precision of the obtained results must be examined and evaluated at the post-processing step, with reference to statistical indicators and independent field measurements. The detailed processing in this study is to be discussed in the following sections.

3.3.1. Pre-Processing Step

At the first step of satellite image analysis, the required pre-processes were applied to the raw S3/OLCI data, including the radiometric and atmospheric corrections. To this end, the ACOLITE module (version: 20220222.0) was selected to perform the atmospheric corrections, where it had been adapted for the processing of the S3/OLCI data over turbid waters, such as those in the study area (Vanhellemont and Ruddick, 2021). In fact, the ACOLITE applies the Dark Spectrum Fitting (DSF) approach, and it is initialized with the assumption that the atmosphere is homogeneous over a captured scene. Although this module has been originally designed for clear waters, it can be recommended for the S3/OLCI data processing in turbid ones as well (Vanhellemont and Ruddick, 2018; Vanhellemont, 2019, 2020; Vanhellemont and Ruddick, 2021). The default output files of the ACOLITE (namely, the L1R and L2R) also include some products, such as the top-of-atmosphere reflectance (ρ_t) and the surface-level reflectance (ρ_s) for all 17 bands of S3/OLCI. However, it is possible to have additional products, such as the surface level reflectance for water pixels (ρ_w) and the remote sensing reflectance (R_{rs}) for water pixels ($R_{rs} = \rho_w/\pi$) if these datasets are requested in advance and before running the module. In this study, the ρ_w values were initially computed, and then applied for further image analysis to determine the Z_{sd} values.

3.3.2. Main-Processing Step

The main-processing step has two parts, including the utilization of an existing algorithm and the development of a novel one to compute the Z_{sd} values from the S3/OLCI data. The applied existing

empirical method had been thus proposed by Doron et al. (2011), while its basic concept had been formerly developed in Doron et al. (2007). The concept of the proposed model is based on utilizing *R*(490), *R*(560), and their ratio values to calculate the Z_{sd} values for both procedures. As mentioned before, a total number of 114 field-observed Z_{sd} values during the first seven cruises were employed for the calibration of the model, and then the other 43 data of the eighth cruise were utilized for the accuracy assessment and validation of the results. Afterward, the optimum model was selected according to statistical indicators, including R^2, RMSE, and MAPE. However, all 157 field measurements were involved to construct the final model after the optimized one was suggested.

3.3.2.1. Using an Existing Model to Calculate Z_{sd} Values from S3/OLCI Data

Upon conducting the pre-processing analysis on the raw S3/OLCI data and at the beginning of the main-processing step, the primary Z_{sd} values were computed in accordance with an empirical method, developed by Doron et al. (2007, 2011). They had established this model out of the simplicity and direct linking of the *R*(490) and *R*(560) values to the Z_{sd} ones. In doing so, the Z_{sd} values could be determined by Eq. 1, as follows:

$$Z_{sd} = 1.888_0(\frac{R(0^-,490)}{R(0^-,560)} \text{-0.52}) \quad (1)$$

where, γ_0 stands for the coupling constant, which can be computed by Eq. 2:

$$_0 = \ln\left(\frac{C_0}{C_{min}}\right)$$

2

in which, C_0 (the inherent contrast) which depends on the optical properties of the Secchi disk and the background water column, can be estimated by Eq. 3:

$$C_0 = \frac{R_{sd} - R_\infty}{R_{sd}}$$

3

where R_{sd} shows the reflectance of the submerged Secchi disk, and R_∞ represents the reflectance of the environment. In this study, R_{sd}=0.85, given the high reflectiveness of the white Secchi disk (Preisendorfer, 1986). Moreover, the R_∞ and C_{min} values (that is, the threshold or liminal contrast of the disk) are considered as 0.02 and 0.01, respectively, based on the average optical properties of water in the study area. Subsequently, the γ_0 value is computed as 8.33, following the insertion of the mentioned values in Eq. 3, and then in Eq. 2.

Subsequently, the $R(0^-, 490)$ and $R(0^-, 560)$ (as the diffuse reflectance at null depth or the irradiance reflectance just below the surface of the B_4 and B_6 bands of S3/OLCI, respectively) can be computed by Eq. 4:

$$R(0^-, \lambda) = \frac{Q\rho_w^\lambda}{\pi_0 + Qr\rho_w^\lambda}) \quad (4)$$

in which, $\Re_0$=0.529, Q = 4, and r = 0.48.

This means that Eq. 4 can be written as Eq. 5 below:

$$R(0^-, \lambda) = \frac{4\rho_w^\lambda}{1.662 + 1.92\rho_w^\lambda}$$

5

Eventually, upon the insertion of the computed $R(0^-, 490)$ and $R(0^-, 560)$ from $\rho_w{}^{490}$ and $\rho_w{}^{560}$ values in Eq. 5, the Z_{sd} values might be determined by applying Eq. 1. To avoid negative and ambiguous values in the computations, a three-step quality control should be done in advance, before applying Eq. 1, consisting of the following criteria:

1. $0.005 < R(0^-,490) < 0.22$,
2. $0.006 < R(0^-,560) < 0.3$, and
3. $0.22 < R(0^-,560)/R(0^-,490) < 3.5$.

3.3.2.2. Proposing a Regional Empirical Model to Calculate Z_{sd} Values from S3/OLCI Data

Since most of the existing algorithms are calibrated based on the global or regional field-measured/observed data, utilizing them for other regions may not be accurate enough, i.e., the development of regional algorithms is not evitable. In this study, it was decided to propose a regional empirical model for the estimation of the Z_{sd} values from the S3/OLCI data based on the $R(490)$, $R(560)$ of the S3/OLCI data (and their ratio values) as well as the field-observed Z_{sd} values, to indicate the optimum model. As mentioned before, the optimum model was selected in accordance with the statistical indicators resulted from independent field measurements, and then the total number of 157 field-observed Z_{sd} values were involved to construct the final model.

3.3.3. Post-Processing Step

The efficiency of the above-mentioned existing and proposed methods was evaluated by statistical indicators, including R^2, RMSE, and MAPE, where:

$$R^2 = \frac{\left(n\sum_{i=1}^{n} Z_{sd}^{FO} \times Z_{sd}^{M} - \sum_{i=1}^{n} Z_{sd}^{FO} \times \sum_{i=1}^{n} Z_{sd}^{M}\right)^2}{\left(n\sum_{i=1}^{n}\left(Z_{sd}^{FO}\right)^2 - \left(\sum_{i=1}^{n} Z_{sd}^{FO}\right)^2\right) \times \left(n\sum_{i=1}^{n}\left(Z_{sd}^{M}\right)^2 - \left(\sum_{i=1}^{n} Z_{sd}^{M}\right)^2\right)}$$

6

,

$$RMSE = \sqrt{\frac{\sum_{i=1}^{n}\left(Z_{sd}^{FO} - Z_{sd}^{M}\right)^2}{n}}$$

7

, and

$$MAPE\,(\%) = 100 \times \frac{1}{n}\sum_{i=0}^{n}\left|\frac{Z_{sd}^{FO} - Z_{sd}^{M}}{Z_{sd}^{M}}\right|$$

8

in which *n* refers to the number of the field-observed Z_{sd} values in the eighth cruise (n = 43), Z_{sd}^{FO} represents the field-observed Z_{sd} values, and Z_{sd}^{M} stands for the modeled Z_{sd} ones. Of note, R^2 measures how well a statistical model predicts an outcome, where the values closer to 1 denote a more proportional model. On the other hand, the smaller RMSE values indicate the higher accuracy of the estimator. MAPE is also the most common measure used to forecast errors, where it is scaled to percentage units and is easier to compare the accuracy of models.

4. Results And Discussion

Based on the independent field-observed Z_{sd} values, the results of both aforesaid existing and proposed models were initially presented, and then compared to select the optimum method for the estimation of the Z_{sd} values from the OLCI/S3 data in the PG&GO. Furthermore, the accuracy of the selected optimized model was assessed by the cross-checking of the results obtained from the overlapped S3 (A&B) images. Finally, the spatiotemporal variation of water transparency in the study area was measured according to the modeled Z_{sd} values acquired from the level-3 monthly climatology remote-sensing reflectance of the S3A/OLCI data.

4.1. Optimum Model Selection

Figure 2a and b illustrate the linear regression between the Ln(Z_{sd}) values in all 157 field-observed points and the absolute/ratio values of *R(i)*, where *i* refers to the S3/OLCI bandwidth. In this respect, among the visible red, green, and blue (RGB) bands of S3/OLCI, the most correlated bands and the band ratio to the Z_{sd} values are OLCI_B_4, OLCI_B_6, and their ratio values based on the R^2 values. This means that

incorporating the OLCI_B_8 (that is, the red band) into the computations brings no significant benefits, so it should be eliminated from the further analysis of the proposed model. Thereafter, two methods were selected to be examined in this research, including a linear and a combined linear and ratio model, both formed by incorporating the B_4 and B_6 bands (Eq. 9):

$$Ln\left(Z_{sd}\right)=a\frac{B_4}{B_6}+bB_4+cB_6+d$$

9

The unknown parameters (a-c) of both models were further calculated by regression analysis and just involving the aforementioned 114 selected points for calibration purposes. Consequently, the final linear (Eq. 10) and combined linear and ratio (Eq. 11) models were formed to compute the Z_{sd} values from the B_4 and B_6 bands.

$$Ln\left(Z_{sd}\right)=28.023B_4-45.82B_6-2.901$$

10

and

$$Ln\left(Z_{sd}\right)=1.673\frac{B_4}{B_6}-1.318B_4-19.992B_6+1.273$$

11

Thereafter, the above-mentioned statistical indicators were used to indicate the optimum model, particularly for the estimation of the Z_{sd} values in the PG&GO area. The graphs in Fig. 3 display the field-observed Z_{sd} values vs. the estimated ones, utilizing Doron et al. (2007, 2011) method (Fig. 3a) and two models examined in this research (Fig. 3b and c) together with the calculated values of R^2, RMSE, and MAPE in 43 data points selected for the accuracy assessments of the results. Compared with the method established by Doron et al. (2007, 2011) (Fig. 3a), the statistical indicators demonstrated that the proposed models in this study revealed significantly better results in the PG&GO area (Fig. 3b and c), particularly when it incorporated all terms of three bands and band ratios (Fig. 3c).

Eventually, after indicating the optimum model, it was decided to involve the total number of 157 field-observed Z_{sd} values to form the final one. Accordingly, the model in the form of Eq. 12 was utilized to compute the Z_{sd} values from the S3/OLCI data.

$$Z_{sd}=e^{1.638\frac{B_4}{B_6}-8.241B_4-12.876B_6+1.26}$$

12

Figure 4a and b display two sample maps generated by applying Eq. 12 on the S3/OLCI images for the dates September 14, 2022 (summertime) and January 23, 2022 (wintertime) from the study area. As shown in these maps, compared with the colder month of January, water transparency in the PG and the

Strait of Hormuz (SH) is totally at higher levels in the warm month of September, in agreement with previous studies in this area (Al Kaabi et al., 2016; Kabiri, 2022). However, the Z_{sd} values in the shallow coastal and estuary areas are relatively lower than the offshore ones in both dates, where they are mostly affected by different sources of natural or man-made contaminations entering from the mainland areas, such as river plumes and wastewaters.

4.2. Accuracy Assessment of Z_{sd} Values Estimated by Cross-Checking S3 (A&B) Imager Results

Both S3 (A&B) satellites follow the same sun-synchronous orbit with an inclination of 98.65°, but are 180° out of phase. As per this geometry, the ground footages of the S3 imagers were not the same, however, some overlaps were observed with an almost half-an-hour difference in the study area. Since this time interval was very small, it could be expected that the variation of water transparency in the overlapped area to be negligible between the two images. With this assumption, it was decided to compare the Z_{sd} values in some dates with the proper data (i.e., good atmospheric conditions and minimum clouds) from the overlapped areas in the PG&GO. Figure 5 shows a sample overlapped area between the S3 (A & B) satellites for the date January 22, 2022 in the PG&GO. In the following, the modeled Z_{sd} values are mapped, and their absolute difference are depicted in Fig. 5b, c, and d for the same date. According to Fig. 5d, the difference in the modeled Z_{sd} values is less than 2 m in the bulk of the overlapped area in the PG. However, regarding the results of other dates, this discrepancy is slightly more in the SH (Fig. 5e) and the GO (Fig. 5f) areas. Since the time interval between the overpasses of the S3 (A&B) satellites is not much (30–40 min), these changes cannot occur due to the variation of water quality, but following the uncertainties coming from the atmospheric corrections of both overlapped images, where they are less accurate in the marginal areas.

4.3. A Spatiotemporal Assessment of Modeled Z_{sd} Values in the Study Area

The level-3 monthly climatology remote-sensing reflectance data of S3A/OLCI (for the B_4 [490 nm] and B_6 [560 nm] bands) were downloaded from the NASA ocean color portal (https://oceancolor.gsfc.nasa.gov/l3/) to generate the related Z_{sd} maps. These data are a product formed based on the S3A/OLCI level-2 ones, which are as atmospherically corrected remote-sensing reflectance values. Since the launching date of S3A is two years before S3B, the range of the averaged value is longer and more reliable, and this is why it was utilized in this study. Afterward, the relevant monthly Z_{sd} maps were generated by applying Eq. 12 on the above-mentioned data. Typically, the date range of the data was 2016–2022; however, it was 2017–2022 for January to March, and 2016–2021 for October to December at the time of the study. Accordingly, Fig. 6a shows the Z_{sd} maps generated for all 12 months in the study area. To better analyze the Z_{sd} values, the mean values were computed in three regions,

including the PG, the SH, and the GO. In doing so, the border of the regions was considered with reference to the Flanders Marine Institute, 2020 dataset (Fig. 6b). However, the graphs in Fig. 6c represent the monthly mean value of Z_{sd} in the three mentioned regions. The graphs indicate that water transparency in all three regions in warmer months (May to August) is higher compared to the colder ones (December to March), mostly due to the blowing of the stronger winds in winter, mixing the water layers, and decreasing water transparency (Reynolds, 1993; Thoppil and Hogan, 2010; Ghafarian et al., 2022; Kabiri 2022a). The other results from the graphs suggest that the domain of the annual oscillation of the Z_{sd} values in the GO (5–18 m) is evidently higher compared with those in the PG (4–12 m) and the SH (7–10 m) regions, so the maximum Z_{sd} value in the GO has happened in the warmest month (June) and before the beginning of summer monsoon (after July), which initiates a strong upwelling system in this region (Yi et al., 2018).

5. Conclusion And Summary

In this study, the Z_{sd} values as a measure of water transparency were estimated, using the S3 (A&B) data in the PG&GO. To this end, the capabilities of an existing empirical method together with a novel one proposed here were examined to indicate the optimum model. On the other hand, the field Z_{sd} values, which had been observed during eight research cruises of the whole study area in different seasons between 2018 and 2022, were utilized as the training and control data. The final results demonstrated that the proposed model in this study had better efficiency, compared with the existing empirical one. Afterward, the monthly S3A/L3 data were employed to assess the spatiotemporal variation of water transparency (that is, the modeled Z_{sd} values) in the PG, the SH, and the GO, separately. The results confirmed that the GO had the highest annual oscillation of water transparency, as compared with that in the PG and the SH. However, it was concluded that water transparency in the study area was lower in the colder months (from November to March) due to the well-mixing of the water columns caused by stronger winds in wintertime, and subsequently decreasing water transparency.

Declarations

Ethical Approval

The author declare that I have no known competing financial interests or personal relationships that could have appeared to influence the work reported in this paper.

Consent to Participate

Not applicable.

Consent to Publish

Not applicable.

Authors Contributions

Conception, design, material preparation, data collection, and analysis were performed by K. Kabiri.

Competing Interests

Not applicable.

Availability of data and materials

Not applicable.

Funding

Not applicable.

References

1. Akhyani M, Chegini V, Bidokhti AA (2015) An appraisal of the power density of current profile in the Persian Gulf and the Gulf of Oman using numerical simulation. Renewable Energy 74:307–317
2. Al Kaabi MR, Zhao J, Charron C, Gherboudj I, Lazzarini M, Ghedira H (2013), September Developing satellite-based tool for water turbidity mapping in the Arabian Gulf: Abu Dhabi case study. In *2013 OCEANS-San Diego* (pp. 1–4). IEEE
3. Al Kaabi M, Zhao J, Ghedira H (2016) MODIS-based mapping of Secchi disk depth using a qualitative algorithm in the shallow Arabian Gulf. Remote Sens 8(5):423
4. Alikas K, Kratzer S (2017) Improved retrieval of Secchi depth for optically-complex waters using remote sensing data. Ecol Ind 77:218–227
5. Beni AN, Marriner N, Sharifi A, Azizpour J, Kabiri K, Djamali M, Kirman A (2021) Climate change: A driver of future conflicts in the Persian Gulf Region?.Heliyon, 7(2), e06288
6. Chen Z, Muller-Karger FE, Hu C (2007)Remote sensing of water clarity in Tampa
7. Doron M, Babin M, Hembise O, Mangin A, Garnesson P (2011) Ocean transparency from space: Validation of algorithms estimating Secchi depth using MERIS, MODIS and SeaWiFS data. Remote Sens Environ 115(12):2986–3001
8. Doron M, Babin M, Mangin A, Hembise O (2007) Estimation of light penetration, and horizontal and vertical visibility in oceanic and coastal waters from surface reflectance. J Geophys Research: Oceans 112:C6
9. Flanders Marine Institute (2020) Union of the ESRI Country shapefile and the Exclusive Economic Zones (version 3). Available online at https://www.marineregions.org/. https://doi.org/10.14284/403. Consulted on 2021-08-16

10. Ghafarian P, Kabiri K, Delju AH, Fallahi M (2022) Spatio-temporal variability of dust events in the northern Persian Gulf from 1991 to 2020. Atmospheric Pollution Research. 101357https://doi.org/10.1016/j.apr.2022.101357
11. Kabiri K (2022a) Estimation of the Secchi disk depth from the NASA MODIS-Aqua diffuse attenuation coefficient data in the northern Persian Gulf and the Gulf of Oman: A spatiotemporal assessment. Reg Stud Mar Sci 52:102359
12. Kabiri K (2022b) Remote sensing of water clarity in the near-shore zone using a cross-sensor-based method: feasibility study: Kish Island, Persian Gulf. J Coastal Conserv 26(4):1–15
13. Kabiri K, Moradi M (2016) Landsat-8 imagery to estimate clarity in near-shore coastal waters: feasibility study-Chabahar Bay, Iran. Cont Shelf Res 125:44–53
14. Kabiri K, Pradhan B, Samimi-Namin K, Moradi M (2013) Detecting coral bleaching, using QuickBird multi-temporal data: a feasibility study at Kish Island, the Persian Gulf. Estuar Coast Shelf Sci 117:273–281
15. Kabiri K, Rezai H, Moradi M (2018) Mapping of the corals around Hendorabi Island (Persian Gulf), using Worldview-2 standard imagery coupled with field observations. Mar Pollut Bull 129(1):266–274
16. Kataržytė M, Vaičiūtė D, Nasvytis P (2019) Excellent bathing waters in coastal areas: is microbial pollution the only important parameter? Ocean & Coastal Management 182:104922
17. Kloiber SM, Brezonik PL, Olmanson LG, Bauer ME (2002) A procedure for regional lake water clarity assessment using Landsat multispectral data. Remote Sens Environ 82(1):38–47
18. Kratzer S, Håkansson B, Sahlin C (2003) Assessing Secchi and photic zone depth in the Baltic Sea from satellite data.Ambio,577–585
19. Kyryliuk D, Kratzer S (2019) Evaluation of Sentinel-3A OLCI products derived using the Case-2 Regional CoastColour processor over the Baltic Sea. Sensors 19(16):3609
20. Luis KM, Rheuban JE, Kavanaugh MT, Glover DM, Wei J, Lee Z, Doney SC (2019) Capturing coastal water clarity variability with Landsat 8. Mar Pollut Bull 145:96–104
21. McCullough IM, Loftin CS, Sader SA (2012) Combining lake and watershed characteristics with Landsat TM data for remote estimation of regional lake clarity. Remote Sens Environ 123:109–115
22. Moradi M, Kabiri K (2015) Spatio-temporal variability of SST and Chlorophyll-a from MODIS data in the Persian Gulf. Mar Pollut Bull 98(1–2):14–25
23. Olmanson LG, Bauer ME, Brezonik PL (2008) A 20-year Landsat water clarity census of Minnesota's 10,000 lakes. Remote Sens Environ 112(11):4086–4097
24. Olmanson LG, Brezonik PL, Finlay JC, Bauer ME (2016) Comparison of Landsat 8 and Landsat 7 for regional measurements of CDOM and water clarity in lakes. Remote Sens Environ 185:119–128
25. Preisendorfer RW (1986) Secchi disk science: Visual optics of natural waters 1. Limnol Oceanogr 31(5):909–926

26. Qin Z, Wen Y, Jiang J, Sun Q (2023) An improved algorithm for estimating the Secchi disk depth of inland waters across China based on Sentinel-2 MSI data.Environmental Science and Pollution Research,1–16
27. Ren J, Zheng Z, Li Y, Lv G, Wang Q, Lyu H, …, Bi S (2018) Remote observation of water clarity patterns in Three Gorges Reservoir and Dongting Lake of China and their probable linkage to the Three Gorges Dam based on Landsat 8 imagery. Sci Total Environ 625:1554–1566
28. Reynolds RM (1993) Physical oceanography of the Gulf, Strait of Hormuz, and the Gulf of Oman—Results from the Mt Mitchell expedition. Mar Pollut Bull 27:35–59
29. Swift TJ, Perez-Losada J, Schladow SG, Reuter JE, Jassby AD, Goldman CR (2006) Water clarity modeling in Lake Tahoe: Linking suspended matter characteristics to Secchi depth. Aquat Sci 68(1):1–15
30. Thoppil PG, Hogan PJ (2010) Persian Gulf response to a wintertime shamal wind event. Deep Sea Res Part I 57(8):946–955
31. Toming K, Kutser T, Uiboupin R, Arikas A, Vahter K, Paavel B (2017) Mapping water quality parameters with sentinel-3 ocean and land colour instrument imagery in the Baltic Sea. Remote Sens 9(10):1070
32. Tyler JE (1968) The secchi disc. Limnol Oceanogr 13(1):1–6
33. Vanhellemont Q (2019) Adaptation of the dark spectrum fitting atmospheric correction for aquatic applications of the Landsat and Sentinel-2 archives. Remote Sens Environ 225:175–192
34. Vanhellemont Q (2020) Sensitivity analysis of the dark spectrum fitting atmospheric correction for metre-and decametre-scale satellite imagery using autonomous hyperspectral radiometry. Opt Express 28(20):29948–29965
35. Vanhellemont Q, Ruddick K (2018) Atmospheric correction of metre-cale optical satellite data for inland and coastal water applications. Remote Sens Environ 216:586–597
36. Vanhellemont Q, Ruddick K (2021) Atmospheric correction of Sentinel-3/OLCI data for mapping of suspended particulate matter and chlorophyll-a concentration in Belgian turbid coastal waters. Remote Sens Environ 256:112284
37. Wu G, De Leeuw J, Skidmore AK, Prins HH, Liu Y (2008) Comparison of MODIS and Landsat TM5 images for mapping tempo–spatial dynamics of Secchi disk depths in Poyang Lake National Nature Reserve, China. Int J Remote Sens 29(8):2183–2198
38. Yang L, Yu D, Yao H, Gao H, Zhou Y, Gai Y, …, Pan S (2022) Capturing Secchi disk depth by using Sentinel-2 MSI imagery in Jiaozhou Bay, China from 2017 to 2021. Mar Pollut Bull 185:114304
39. Yi X, Hünicke B, Tim N, Zorita E (2018) The relationship between Arabian Sea upwelling and Indian Monsoon revisited in a high resolution ocean simulation. Clim Dyn 50(1):201–213

Figures

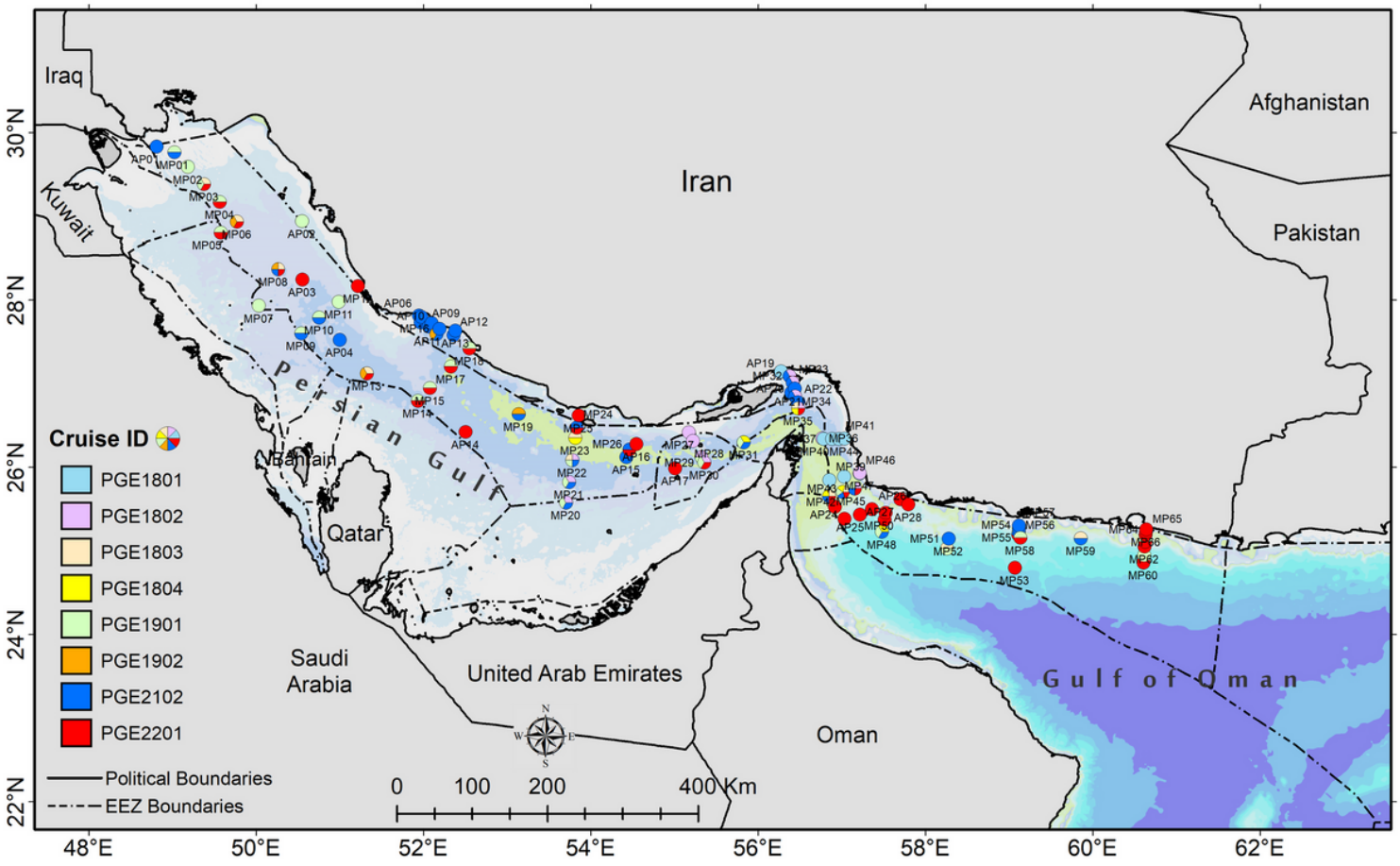

Figure 1

The location of point field observations during eight cruises operated by the research vessel, the PGE, in the PG&GO between 2018 and 2022 (some points are observed in two or more cruises)

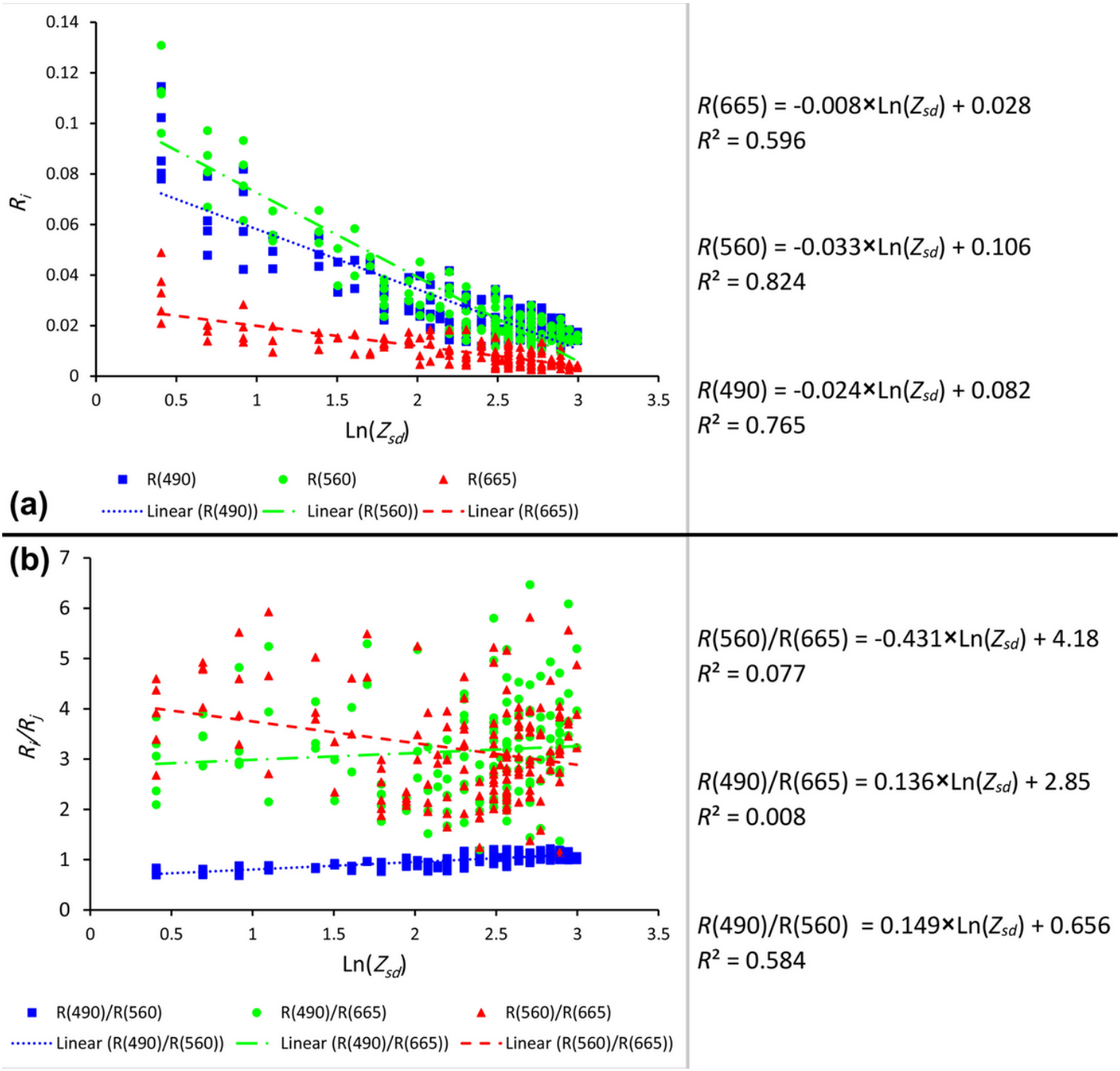

Figure 2

The correlation between bands (a) and band ratios (b) of the S3/OLCI and Ln(Z_{sd}) values. Based on the R^2 values, the most correlated bands/band ratios are B_6 (560 nm), B_4 (490 nm), and their ratio values.

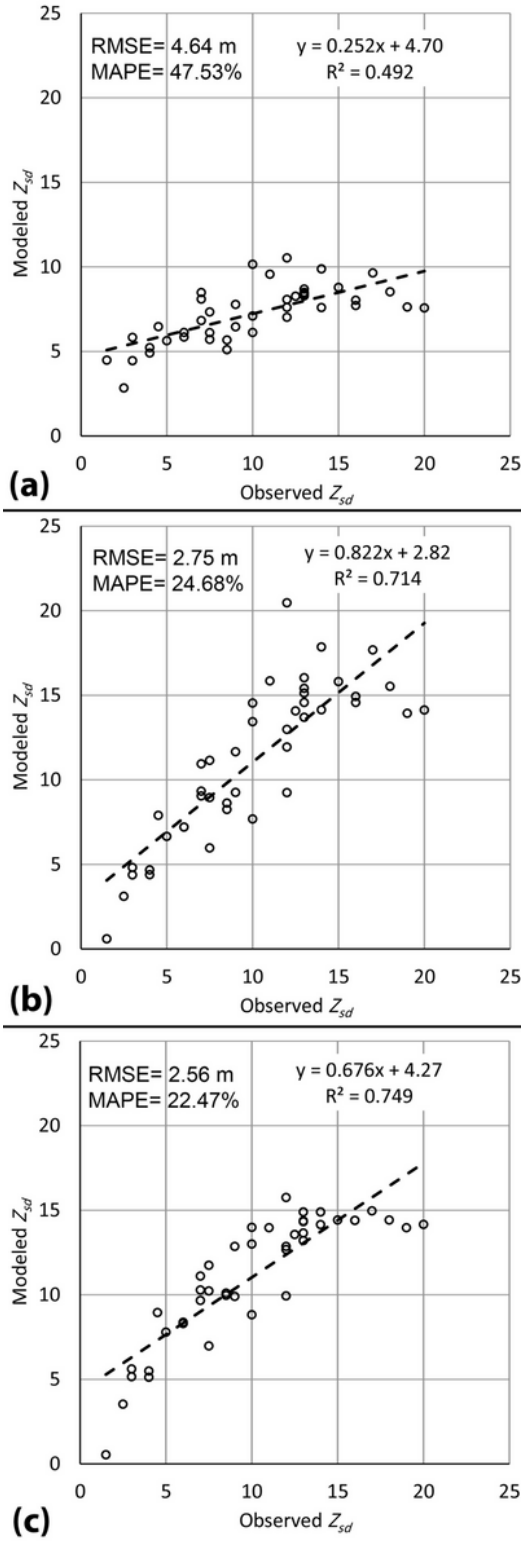

Figure 3

The relationship between the modeled and observed Z_{sd} values in the points selected for validation analysis (n=43) of the model based on the method developed by Doron et al. (2007, 2011) (a), the linear model (b), and combined linear and ratio model (c), examined in this study

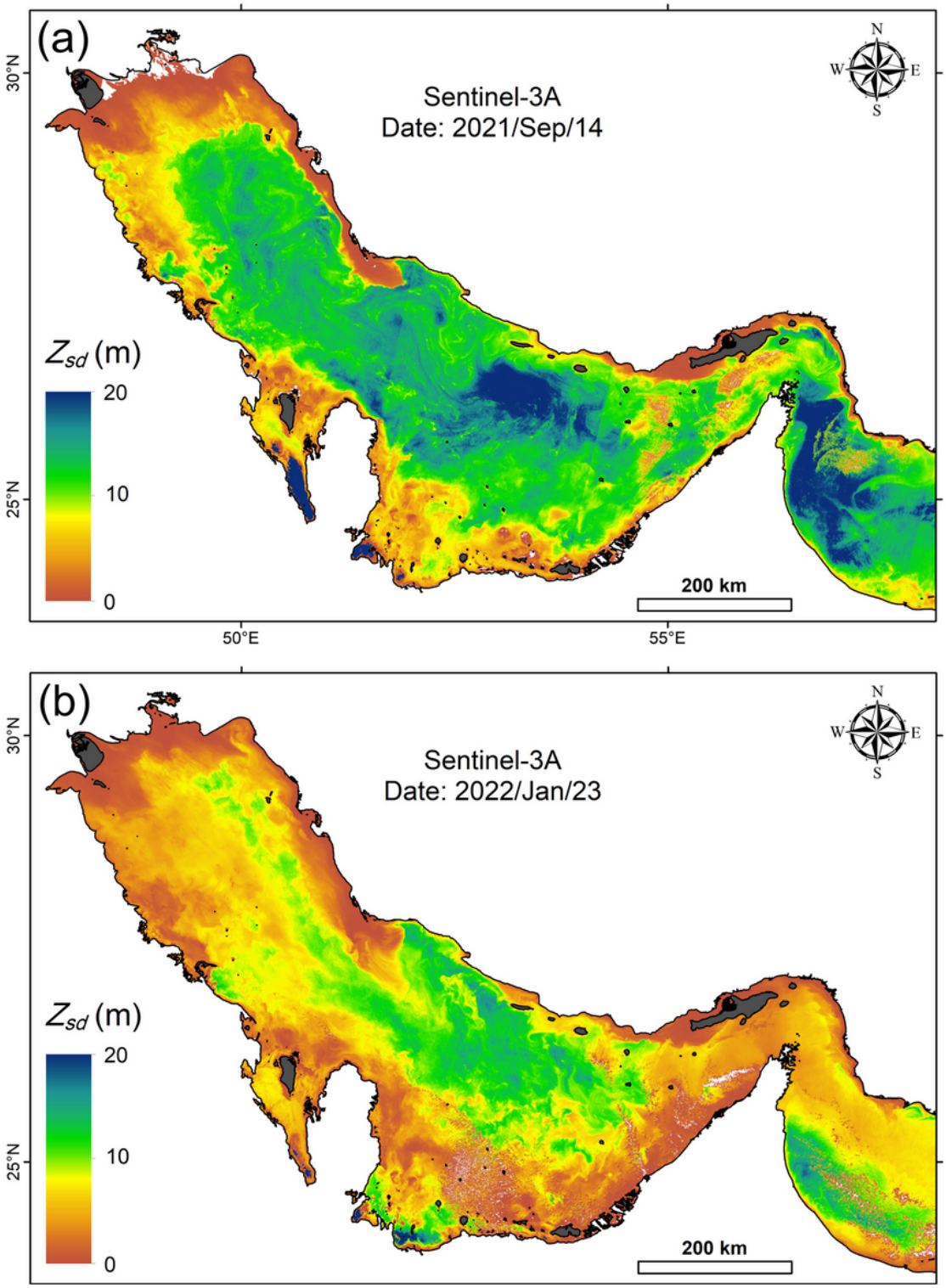

Figure 4

The sample maps generated by the model proposed in this study for September 14, 2022 (a), and January 23, 2022 (b). Generally, water transparency in warmer months is higher compared with the colder ones in the study area.

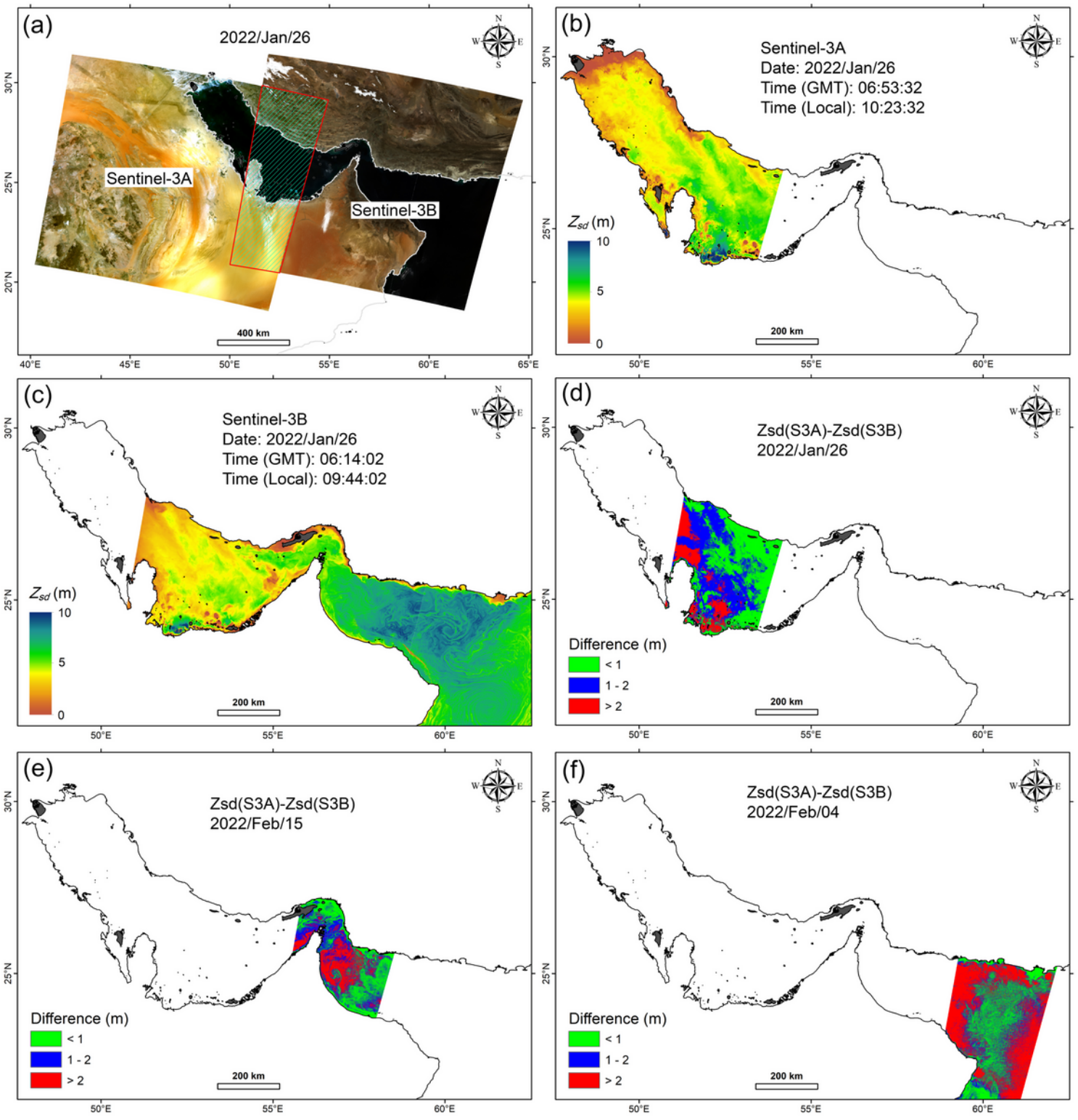

Figure 5

An overlapped area between S3 (A&B) satellites for January 22, 2022, in the PG&GO (a). The modeled Z_{sd} values for S3A (b), S3B (c), and their absolute difference (d). Compared with the PG, this difference is higher in the SH (e) and the GO (f) areas.

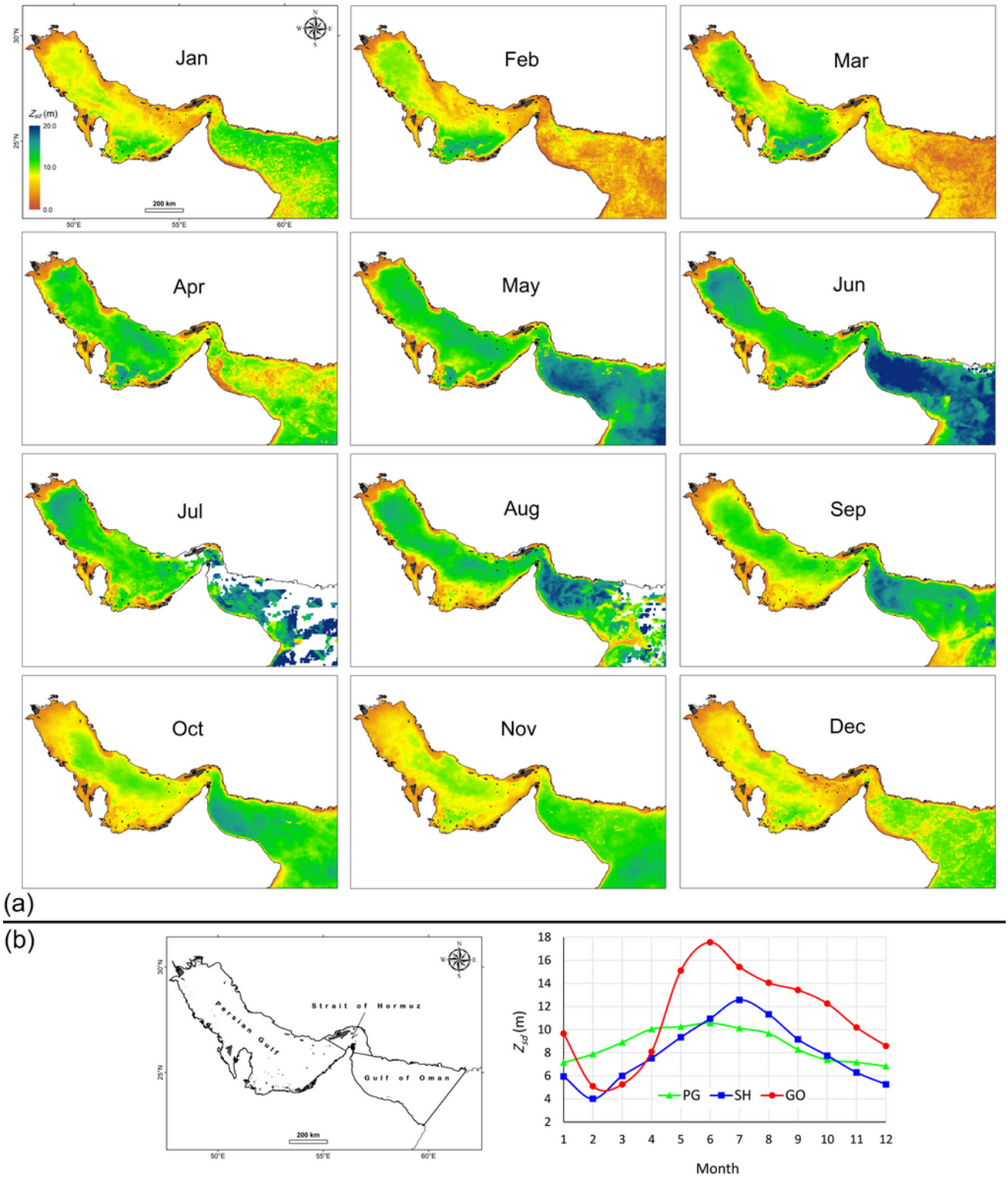

Figure 6

The distribution pattern of modeled mean monthly Z_{sd} values in the PG&GO between 2016 and 2022 (a). The graph showing the mean values of three regions (b). The border of regions considered based on the Flanders Marine Institute, 2020 dataset